Supplementary materials

for

Design of experiments (DoE) to develop and to optimize extraction of psychoactive substances

Tiantian Tang[a, 1], **Wanyi Chen**[a, 1], **Lixian Li**[a], **Shurui Cao**[b, c, *]

[a]*Department of Pharmacy, Chongqing University Cancer Hospital, Chongqing 400030, China*

[b]*Forensic Identification Center, Southwest University of Political Science and Law, Chongqing 401120, China*

[c]*Criminal Investigation Law School, Southwest University of Political Science and Law, Chongqing 401120, China*

S1. Supporting Material for Experimental

S1.1. Standard solutions and reagents

Standard solutions (1 mg mL^{-1}) of ephedrine (EPH), methylephedrine (MEEP), amphetamine (AMP), methamphetamine (MEAM), morphine (MOR), papaverine (PAP), and thebaine (THE) were purchased from Anpel Laboratory Technologies Inc. (Shanghai, China). The information of seven PAS was shown in Table S1. Graphene oxide powder was bought from Jining Leader Nano Technology Co., Ltd. (Shandong, China). ZIF-8 was obtained from J&K Scientific Ltd. (Shanghai, China). $FeCl_3•6H_2O$ and $FeCl_2•4H_2O$ were purchased from Macklin Biochemical Co., Ltd. (Shanghai, China). NaCl, NaOH, HCl, $NH_3•H_2O$, ethanol, methanol, acetonitrile, and other analysis reagents were sourced from Tedia (Fairfield, OH, USA).

S1.2. Preparation of adsorbent

The Fe_3O_4/GO/ZIF-8 (MGZ) was prepared according to our previous work.[1] The Fe_3O_4/GO (MG) was prepared by the chemical coprecipitation method. Firstly, 0.15 g GO powder was dispersed in 100 mL deionized water and then sonicated for 1 h. Under N_2 atmosphere, 1.8 g $FeCl_3•6H_2O$ and 0.8g $FeCl_2•4H_2O$ were dissolved in 25 mL ultrapure water. Secondly, the GO dispersion was quickly added into the above Fe salt mixture and stirred vigorously at 80 °C for 1 h.

***Corresponding author: Shurui Cao**
E-mail address: caoshurui@yeah.net

1 The author contributed equally to the work

Thirdly, 10 mL ammonia solution was added into the mixed system and kept stirring for 30 min. After completed the reaction, the product MG was collected by an external magnet and washed several times with ethanol and water.

Fe_3O_4/GO/ZIF-8 (MGZ) was synthesized through a facile self-assembly method. MG was prepared into a dispersion with the concentration of 1 mg mL^{-1} and then dropwise added into the dispersion solution containing appropriate amounts of ZIF-8 under stirring. Finally, moderate stirring was continued for 24 h and then washed and dried. All products were dried in vacuum (XFL 050, FranceEtuves, France) at 60 °C.

S1.3. Material characterization

The scanning electron microscopy (SEM) (Genimi 500, Zeiss, Germany) and transmission electron microscopy (TEM) (G2F20, FEI, USA) at different magnifications was used to observe the morphology of prepared materials. Energy-dispersive spectroscopy (EDS) analysis was carried out on SEM-EDS spectrometer. The fourier transform infrared spectra (FT-IR) (Nicolet IS10, ThermoFisher, USA, at the range of 4000-400 cm^{-1}), Raman spectra (Renishaw, UK) and X-ray photoelectron spectroscopy (XPS) (Thermo Scientific Escalab 250Xi, ThermoFisher, USA) were conducted to analyze the chemical components and functional groups. The vibrating sample magnetometer (7404, VSM) (Lake Shore, USA) was adopted to resolve the magnetic properties. The specific surface area and pore size distribution of the adsorbents were evaluated by a BELSORP-max analyzer (MicrotracBEL, Japan) utilizing multipoint BET (Brunauer Emmet Teller) and BJH (Barret-Joyner-Halenda) method.

S1.4. Adsorption experiments

The batch adsorption experiments were conducted to evaluate the adsorption behavior of seven PAS on MGZ adsorbent, including adsorption kinetics and equilibrium. Traditionally, 15 mg of adsorbent was mixed into 3 mL of PAS mixed solution with a concentration range of 0-500 μg L^{-1}. The mixture was placed in a shaker incubator (SKY 2112B, Shenzhen, China) with stirring at 110 rpm for 0-400 min. All adsorbent separation was carried out at the end of the process by using an external magnet. Finally, the mixture solution was filtered through a 0.22 μm membrane before determination. The adsorption capacity (Q), enrichment factor (EF), and recovery (R) for seven PAS were determined using the following *Eq. (1)*, *Eq. (2)*, and *Eq. (3)*, respectively.

$$Q = \frac{(C_0 - C_e)V}{W} \tag{1}$$

$$EF = \frac{C_{elution}}{C_{added}} \tag{2}$$

$$R\ (\%) = \frac{C_{elution}V_{elution}}{C_{added}V_{added}} = \frac{Q_{elution}}{Q_{added}} \times 100\% \tag{3}$$

Where C_0 and C_e (μg L^{-1}) are the concentrations of PAS solution at the initial time and at equilibrium, respectively; V (L) is the volume of the solution and W (g) is the weight of the adsorbent; $C_{elution}$ and C_{added} (μg) are the concentrations of PAS elution and spiked into the matrix samples, respectively. $Q_{elution}$ and Q_{added} (μg) are the amount of PAS elution and spiked into the matrix samples, respectively.

The equations of pseudo-first-order, pseudo-second-order and Elovich models were expressed as follows:

$$log(Q_e - Q_t) = logQ_e - K_1t \tag{4}$$

$$\frac{t}{Q_t} = \frac{1}{K_2Q_e^2} + \frac{t}{Q_e} \tag{5}$$

$$Q_t = \frac{1}{b}lnab + \frac{1}{b}lnt \tag{6}$$

Where Q_t and Q_e (μg g^{-1}) are the quantity of PAS attracted onto the adsorbent surface at the adsorption time t (min) and the equilibrium, respectively. K_1 (min^{-1}) is the constant for rate of adsorption for first order reaction. K_2 (g mg^{-1} min^{-1}) is the constant for rate of adsorption for second order reaction. a (mg g^{-1} min^{-1}) represents the initial rate of adsorption and b (mg g^{-1}) constitutes the extent of the surface coverage and activation energy in the chemisorption mode of interaction between the adsorbate and adsorbent.

The equations of Langmuir, Freundlich and Temkin models were shown as follows:

$$\frac{C_e}{Q_e} = \frac{1}{K_LQ_m} + \frac{C_e}{Q_m} \tag{7}$$

$$logQ_e = logK_F + \frac{1}{n}logC_e \tag{8}$$

$$Q_e = BlnK_T + BlnC_e \tag{9}$$

Where Q_m is the maximum adsorption capacity (μg g^{-1}) and K_L is the affinity constants. C_e represents the equilibrium concentration of PAS (ng mL^{-1}). K_F is the FM adsorption parameter related to the adsorption capacity and *n* is the nonlinearity factor related to the intensity of adsorption.

S2. Supporting Material for Result and discussion

S2.1. Characterization

The morphology and elemental composition of MG and MGZ were characterized by SEM and SEM-EDS techniques. Some smooth, separate, and thick GO sheets were exposed, as shown in Fig. S1A, that were not attached with Fe_3O_4 and ZIF-8 particles. This may be caused by the stacking effects between GO sheets. Compared with MG, the stacking of GO sheets in MGZ was significantly reduced (Fig. S1C). Hardly bulky and separate GO sheets were presented in MGZ, indicating the distribution of Fe_3O_4 and ZIF-8 particles on GO was more evenly distributed and their combination was more closely related. Additionally, a fluffy morphology with more folds and slits was displayed in the image of MGZ. It can be seen from Fig. S1B and D, the existence of N and Zn, derived from ZIF-8, were found in MGZ adsorbent, implying that ZIF-8 was successfully grafted onto GO sheets.

N_2 adsorption isotherms were measured to investigate the porosity properties of the materials (Fig. S2A), and the calculated textural properties were provided in Table S2. For MG, the N_2 adsorption isotherm was the typical type IV (as referred to in the IUPAC definition). The adsorption capacity gradually increased in low p/p^0, indicating that N_2 was adsorbed on the inner surface of the pores, progressing from a single to a multi-layered structure. At the middle pressure, the adsorption capacity continued to increase. The adsorption isotherm rapidly increased as p/p^0 increased, reflecting particle packing of pores.[2, 3] For MGZ, the N_2 adsorption isotherm was also type IV, however, its adsorption capacity rapidly rose between 0.0 and 0.1 of p/p^0. And then, a slow plateau phase was presented after reaching a certain value. This is because the adsorption was controlled by the pore volume of the micropores. Both MGZ and MG had H3 hysteresis loops, indicating aggregation of plate-like particles giving rise to slit-shaped pores.[4] Compared with MG, the hysteresis loop of MGZ appeared later, and the loop was narrower, reflecting the existence of micropores in MGZ. Some reported studies also have evidenced that the new pores could be formed between ZIF-8 and GO sheets.[5, 6] Additionally, hybrid MGZ had a larger specific surface area (207.84 $m^2\ g^{-1}$), larger total pore volume (0.28 $cm^3\ g^{-1}$) and a smaller pore diameter (4.29 nm).

The Raman spectra of MG and MGZ were shown in Fig. S2B. There was a signature peak of Fe_3O_4 at 705 cm^{-1}. The D band and G band peaks were apparent at 1330 cm^{-1} and 1591 cm^{-1}, respectively. The D band is related to the disordered structure of graphene, and the G band arises from in-plane vibrations of sp^2 carbon atoms.[7, 8] The intensity ratios of the D band and the G band (ID/IG) can be used to determine the defects of synthetic adsorbents. The lower ID/IG of MGZ (1.39 vs. 1.42) indicated fewer defects in the C atomic crystal, which was due to the insert and filling of ZIF-8 crystal.

FTIR spectra of MGZ and MG were illustrated in Fig. S2C. Broad bands at approximately 3432 and 1403 cm^{-1} were observed in the samples attributed to the stretching and bending vibrations of O−H (or water molecules).[9] The peaks of GO at 1735, 1634, 2853 and 2924 cm^{-1} observed in the patterns of GO were ascribed to the vibrations of C=O, C=C and C−H bonds.[2] Two peaks at 640 and 592 cm^{-1} were attributed to Fe−O bonds. These peaks were both existed in the MGZ and MG, indicating the magnetic materials were successfully prepared. The characteristic peaks of C=N, C−N and Zn−N bonds at 1577, 1147 and 422 cm^{-1}, respectively, belonging to the imidazole ring of ZIF-8.[10] Additionally, the bands at 600-800 cm^{-1} were attributed to the out of plane vibration of imidazole ring and bands appeared at 900-1350 cm^{-1} were corresponded to the in-plane bending of the imidazole ring.[11] These results were consistent with the characteristic peaks of ZIF-8,[12, 13] demonstrating the incorporation of ZIF-8 crystals into the MG. Table S2 displayed information on characteristic peaks, indicating that the MG was successfully prepared and the ZIF-8 was successfully grafted on the MG.

The magnetization curves of the adsorbents were compared in Fig. S2D. The saturation magnetization of MGZ (41 emu g^{-1}) was lower than that of MG (60 emu g^{-1}). This was due to the introduction of non-magnetic ZIF-8. MGZ could be easily separated using a magnet, making it a promising candidate for extraction with great separability and recycleability.

S2.2. Adsorption experiments

Adsorption kinetics contain important information about solute uptake rate at the interface of a solid-solution system and provide beneficial details corresponding to the pathways and mechanisms of reaction. Pseudo-first-order,[14] pseudo-second-order,[15] and Elovich[16] models were conducted to analyze the kinetic adsorption of seven PAS onto the MGZ. The interactions, adsorption capacity, and procedure energy during the adsorption process could be studied by an adsorption isotherm. Therefore, the adsorption data were fitted using three isotherm models, including Langmuir,[17] Freundlich,[18] and Temkin,[19] for the description of the PAS adsorption process onto the MGZ. The equations of the kinetic and isothermal models were represented in the supplemental materials.

The non-linear kinetic fitting curves of the kinetic models were given in Fig. S5 (A–G). As contact time increased, the adsorption capacity of seven PAS increased. The adsorption process was divided into two stages: (1) the rapid process during the 0-100 min, which was due to the existence of abundant unoccupied active sites and weaker resistance. (2) Slow stage after 100 minutes as a result of the rapidly decreasing adsorption rate, which gradually reached equilibrium with the saturation effect. The parameters of the fitting results were exhibited in Table S5. The Elovich model could better describe the kinetic data because it had greater non-linear correlation coefficients (R^2 = 0.945-0.997) than those of other kinetic models. This suggested that the solid surface-active sites were energetically heterogeneous in nature. And chemisorption played a vitally important role in the PAS adsorption process.[20] Due to the self-assembly effect, ZIF-8 particles were randomly distributed on the surface of the MG, forming an inhomogeneous adsorption interface. Moreover, based on the multifunctional functional groups of GO (−COOH, −OH, π-electron system) and active sites of ZIF-8 (imidazole ring and Zn^{2+}), the adsorption interface exhibited different energy intensities, which was consistent with the assumption of the Elovich model.

As portrayed in Fig. S5H-N and Table S6, according to the R^2 values, the Langmuir model (R^2 = 0.995-0.999) was better fitted with the experimental data than the Freundlich (R^2 = 0.989-0.993) and Temkin (R^2 = 0.808-0.888) models for EPH, MEEP, MEAM, and MOR. For AMP, PAP, and THE, the Freundlich model was fitted the best because of the greater R^2 (0.955-0.995), and all values of *1/n* were in the range of 0–1, indicating that favorable heterogeneous adsorption existed in the MSPE process. The theoretical maximum monolayer adsorption capacities of EPH, MEEP, AMP, MEAM, MOR, PAP, and THE by MGZ were 68.047, 48.669, 129.244, 101.096, 103.272, 84.336, and 64.217 $\mu g\ g^{-1}$, respectively. These results indicated that both monolayer adsorption and multilayer adsorption were involved in the adsorption of PAS onto MGZ in the mixed system.[21] On the one hand, a GO with a large specific surface area could provide more contacted sites for attaching PAS molecules to its surface, forming a monolayer adsorption process. On the other hand, many slit pores were formed between MG and ZIF-8, which was beneficial for the diffusion of PAS. Moreover, heterogeneous active sites on the adsorbent surface also provided a platform for multilayer adsorption.

S3. Mechanism for adsorption of PAS

According to the study of the effect of pH on adsorption, hydrogen bonding interactions played an important role in the adsorption of PAS by MGZ. XPS characterization was conducted to further explore the adsorption mechanism. Typically, XPS was used to investigate potential mechanisms of analyte adsorption on an adsorbent. By comparing the XPS spectra of adsorbent and PAS-loaded adsorbent, the changes of chemical elements and chemical bonds were investigated. Fig. S6A and B revealed the XPS survey spectra of MGZ before adsorption and PAS-loaded MGZ. The positions of peaks corresponding to different elements and the relative strengths of peaks (C 1s, N 1s, O 1s, Zn 2p, etc.) could be seen. The content of these elements changed after PAS adsorption, such as 35.6% to 36.3% of C, 12.7% to 14.3% of N, 28.8% to 27.3% of O, 9.2% to 8.7% of Fe, and 13.8% to 13.4% of Zn, indicating that PAS was successfully adsorbed. High resolution XPS spectra of C, N, O, and Zn were depicted in Fig. S6C-J, and relative parameters were concluded in Table S7. The shifting binding energies of the splitting peaks of C, N, O, and Zn indicated the presence of interactions such as π-π stacking, hydrogen bonding, and chelation. This was consistent with the results of the previous adsorption kinetics experiments, suggesting that the adsorption interface was heterogenetic due to the presence of multifunctional groups.

According to the adsorption behavior of the MGZ adsorbent towards the seven PAS, the adsorption performances (Q_m) of the seven PAS decreased in the following order: AMP>MEAM>MOR>PAP>EPH>THE>MEEP. This was due to the difference between the amounts of HBA and HBD as well as their molecular structures. These PAS all have the classic π-electron system as well as nitrogen and/or oxygen elements. Compared with other PAS, owing to the minimal steric hindrance, the adsorption capacity of AMP was the highest. Although the steric hindrances of EPH and MEEP were also small, they were not conducive to the combination with MGZ due to the easy formation of intramolecular hydrogen bonding. For PAP and THE with multiple HBA, the large steric hindrance caused by the multi-ring structure hindered their adsorption onto MGZ, leading to poor adsorption performance.

S4. Box-Behnken design equations

The non-linear quadratic models were shown as following equations.

$$Y_{EPH}=59.91+11.99X_1-7.96X_2-12.88X_3-8.52X_1X_2+2.40X_1X_3+3.70X_2X_3-2.33X_1^2+0.80X_2^2+1.03X_3^2$$

$$Y_{MEEP}=55.09+16.87X_1-8.83X_2-13.51X_3-3.45X_1X_2-4.79X_1X_3+4.03X_2X_3-5.37X_1^2+1.30X_2^2+1.32X_3^2$$

$$Y_{AMP}=90.74+8.44X_1-6.96X_2-5.63X_3+1.36X_1X_2+4.15X_1X_3-1.73X_2X_3-4.87X_1^2-0.21X_2^2+0.19X_3^2$$

$$Y_{MEAM}=92.16+4.94X_1+26.62X_2-3.87X_3+2.94X_1X_2+2.87X_1X_3-2.06X_2X_3-2.48X_1^2-34.00X_2^2-1.40X_3^2$$

$$Y_{MOR}=37.02+12.38X_1+1.94X_2-19.30X_3-3.98X_1X_2-4.31X_1X_3+1.69X_2X_3-1.56X_1^2+0.24X_2^2+8.31X_3^2$$

$$Y_{THE}=60.12+10.09X_1+0.26X_2-15.31X_3-1.51X_1X_2-1.00X_1X_3-2.49X_2X_3-1.42X_1^2-4.99X_2^2+5.17X_3^2$$

Figures and Tables

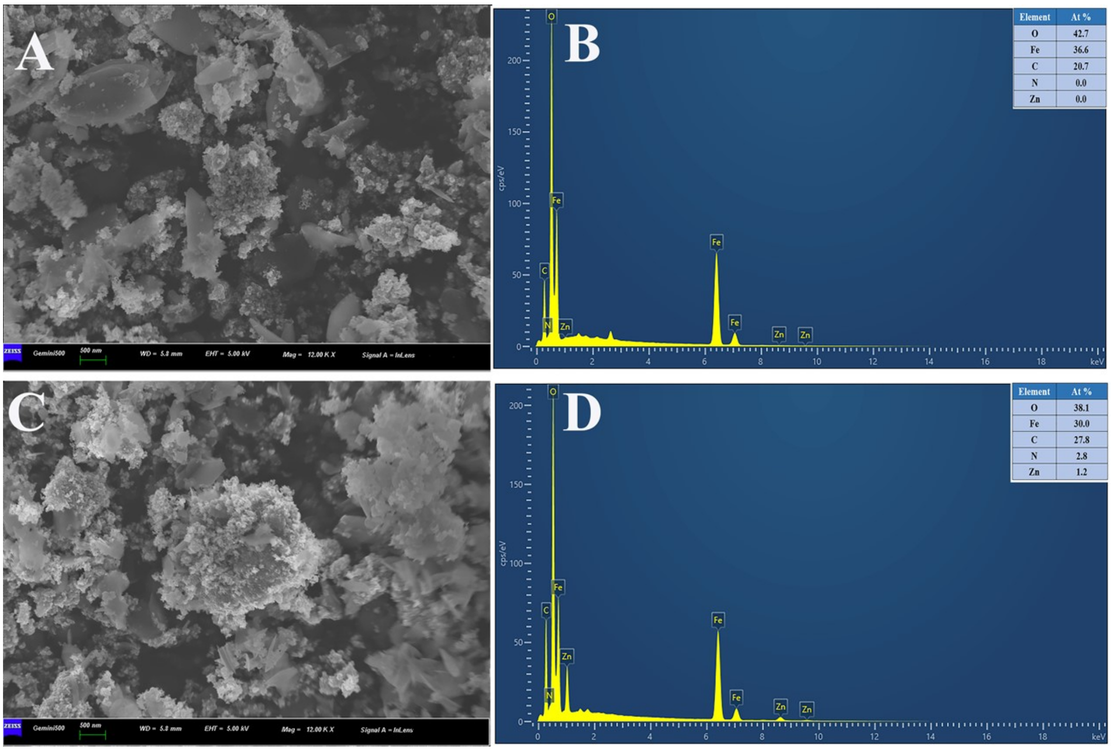

Element	At %
O	42.7
Fe	36.6
C	20.7
N	0.0
Zn	0.0

Element	At %
O	38.1
Fe	30.0
C	27.8
N	2.8
Zn	1.2

Fig. S1 The SEM image of MG (A), and MGZ (B) and the EDS analysis of MG (C) and MGZ (D).

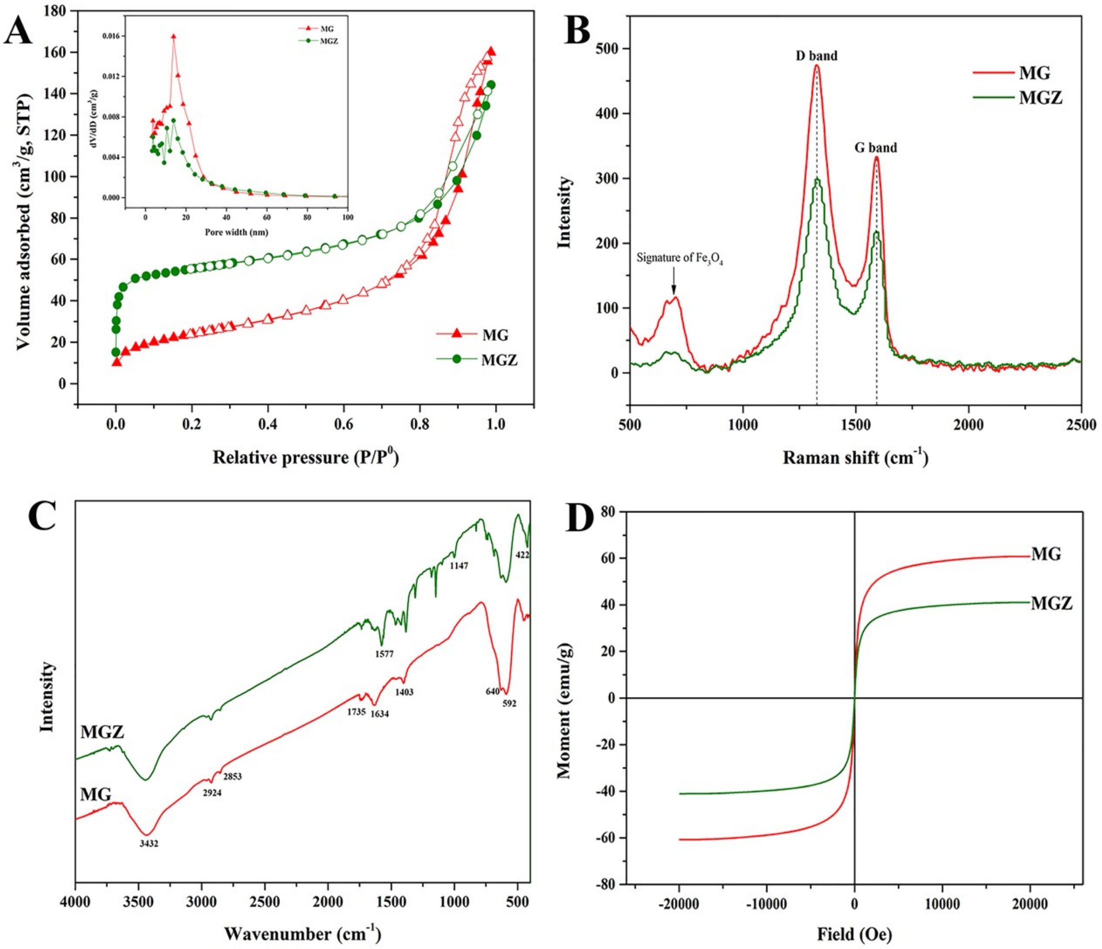

Fig. S2 The N_2 adsorption/desorption isotherms (A), distribution of pore width (insert in A), Raman spectra (B), FTIR spectra (C), magnetization curves (D) of MGZ and MG.

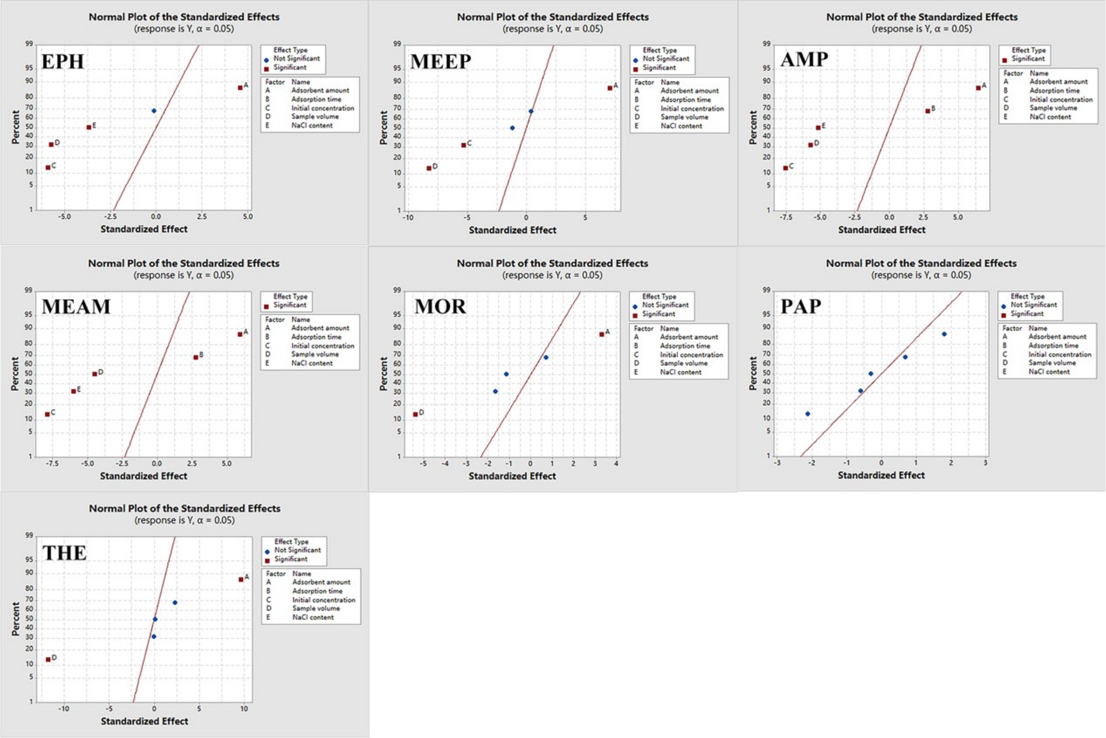

Fig. S3 The Pareto Chart of seven PAS by PBD.

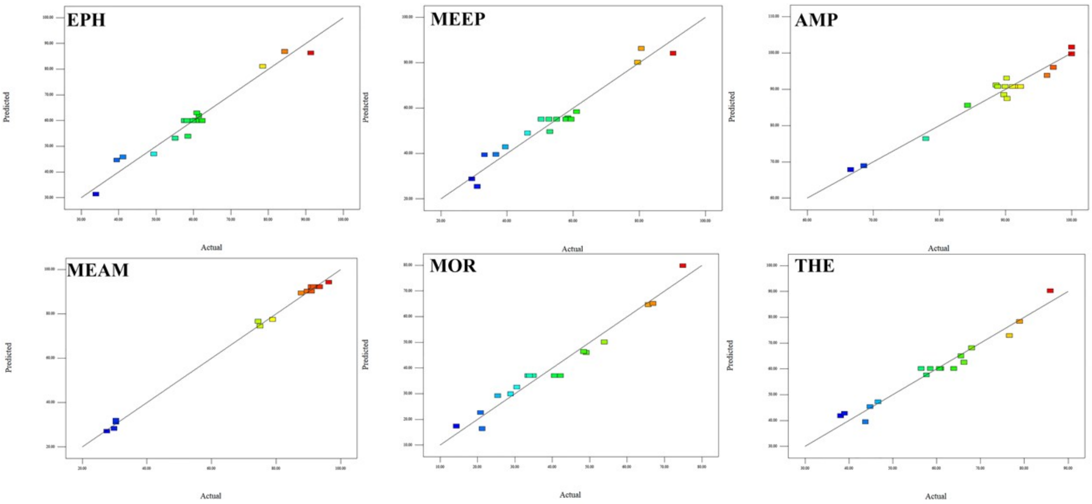

Fig. S4 The distribution of experimental points closed to the regression line (BBD).

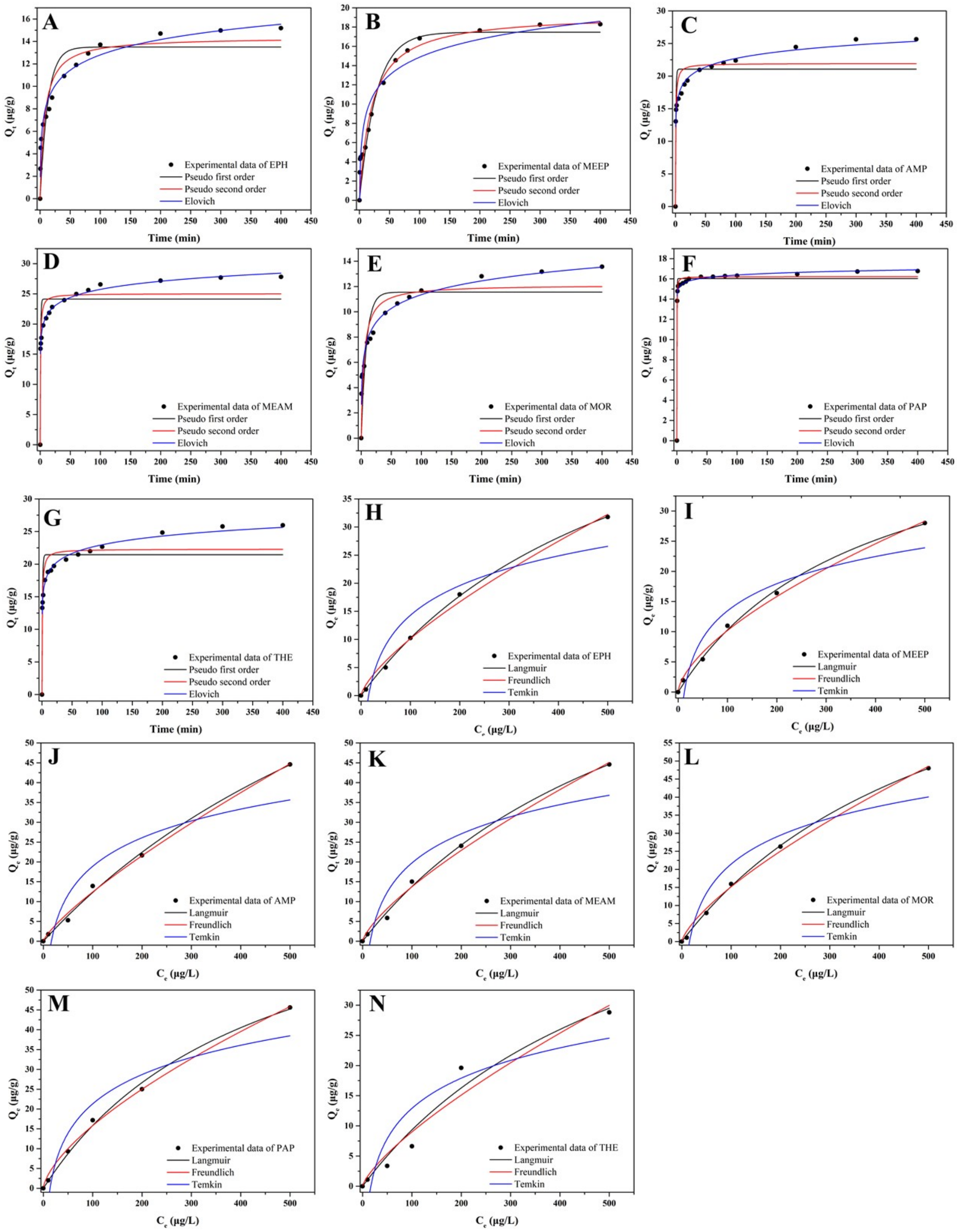

Fig. S5 The Kinetic (A-G) and isotherm (H-N) fitting curves and of seven PAS.

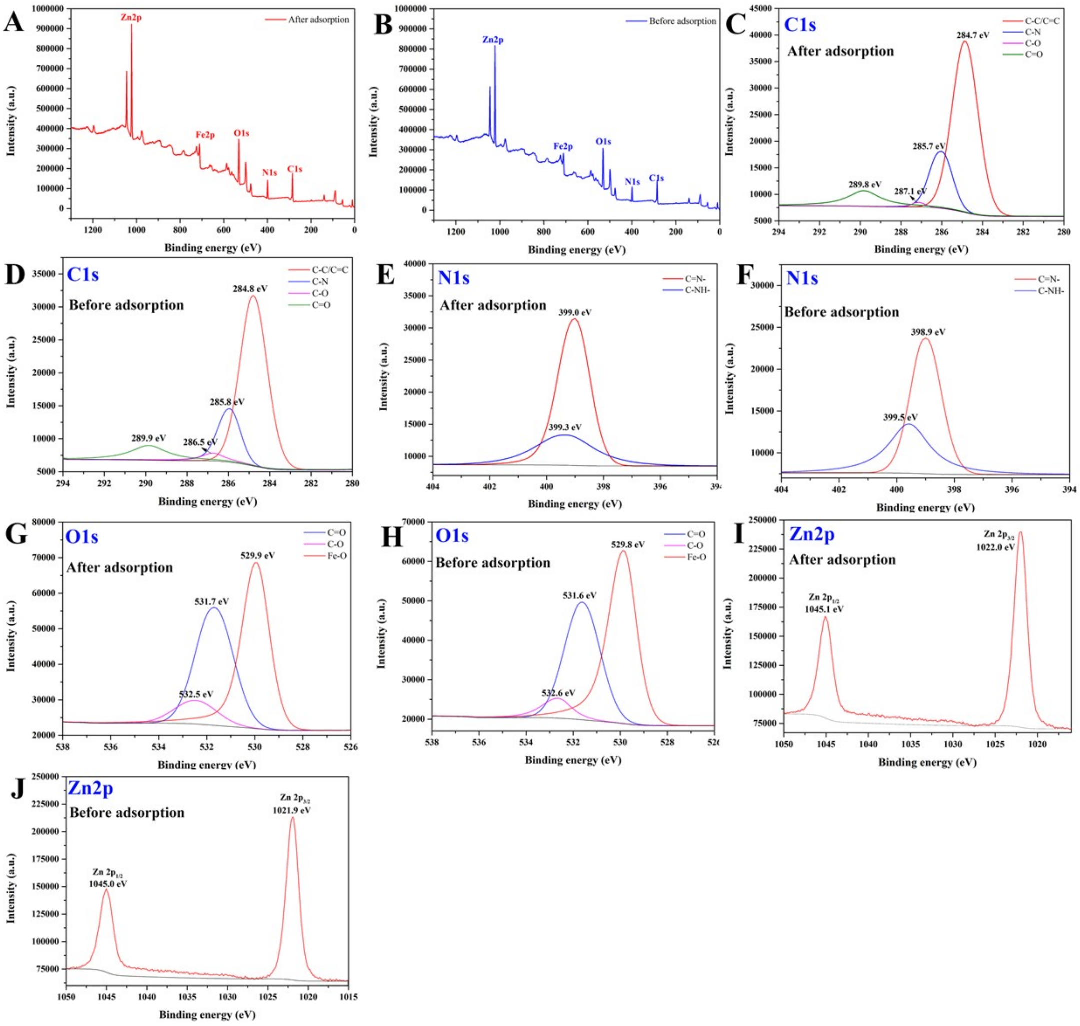

Fig. S6 The XPS spectrum of MGZ after and before adsorption of seven PAS: wide scans (A and B), peaks for C1s, (C and D) peaks for N1s (E and F), peaks for O1s (G and H), and peaks for Zn2p (I and J).

Table S1. The molecules information and multiple reaction monitoring (MRM) parameters of seven psychoactive substances.

Analytes	Molecular formula	Molecular weight	HBD	HBA	pKa	Q_1 (m/z)	Q_3 (m/z)	CE (eV)	DP (eV)
EPH	$C_{10}H_{15}NO$	165.2	2	2	10.3	166.0	147.9*/132.8	10/18	20
MEEP	$C_{11}H_{17}NO$	179.3	1	2	9.3	179.9	146.7/161.9*	12/18	46
AMP	$C_9H_{13}N$	135.2	1	1	10.1	136.1	91.1*/119.1	17/28	15
MEAM	$C_{10}H_{15}N$	149.2	1	1	9.9	150.1	91.1*/119.1	26/16	30
MOR	$C_{17}H_{19}NO_3$	285.3	2	4	8.2	286.0	201.2/165.3*	36/56	80
PAP	$C_{20}H_{21}NO_4$	339.4	0	5	6.4	340.2	202.1*/171.1	36/40	92
THE	$C_{19}H_{21}NO_3$	311.4	0	4	8.2	312	58.2*/251	38/35	52

HBD: Hydrogen bond donor; HBA: Hydrogen bond acceptor; * Quantifying ions.

Table S2. The textural properties and the information of characteristic peaks of MGZ and MG by FTIR analysis.

Textural properties	MGZ	MG
S_{BET} (m^2 g^{-1})	207.84	87.03
V_{mic} (cm^3 g^{-1})	0.06	-
V_T (cm^3 g^{-1})	0.28	0.24
D_p (nm)	4.29	11.37
Wavenumber (cm^{-1})	Chemical bond	Adsorbents
422	Zn−N bending vibration	MGZ
592, 640	Fe−O vibrations	MGZ, MG
600-800	Out of plane of imidozole ring	MGZ
900-1350	In plane of imidozole ring	MGZ
1147	C−N stretching vibration	MGZ
1577	C=N stretching vibration	MGZ
1634	C=C stretching vibration	MGZ, MG
1735	C=O stretching vibration	MGZ, MG
2853, 2924	C−H stretching vibration	MGZ, MG
3432	O−H (or water molecules) stretching vibration	MGZ, MG

S_{BET}: Surface area; V_{mic}: Micropore volume; V_T: Total pore volume; D_p: Average pore diameter.

Table S3. Statistical analysis of five factors using Plackett-Burman design for seven PAS.

Source	D_F	*Adj SS*	*Adj MS*	*F*-Value	*P*-Value
EPH					
Model	6	8.75	1.46	17.72	0.001
Linear	5	8.40	1.68	20.4	0.001
Adsorbent amount (mg)	1	1.73	1.73	21.04	0.004
Adsorption time (min)	1	0.001	0.001	0.02	0.901
Initial concentration (ng mL^{-1})	1	2.87	2.87	34.81	0.001

Sample volume (mL)	1	2.69	2.69	32.68	0.001
NaCl content (mol L^{-1})	1	1.11	1.11	13.44	0.01
Curvature	1	0.36	0.36	4.31	0.083
Error	6	0.49	0.08		
Total	12	9.24			
S	R^2	*Adj-*R^2			
2.87	0.9466	0.8931			
MEEP					
Model	6	10.91	1.82	24.7	0.001
Linear	5	10.85	2.17	29.46	<0.001
Adsorbent amount (mg)	1	3.70	3.70	50.27	<0.001
Adsorption time (min)	1	0.01	0.01	0.17	0.697
Initial concentration (ng mL^{-1})	1	2.05	2.05	27.89	0.002
Sample volume (mL)	1	4.98	4.98	67.62	<0.001
NaCl content (mol L^{-1})	1	0.10	0.10	1.34	0.292
Curvature	1	0.07	0.07	0.89	0.383
Error	6	0.44	0.07		
Total	12	11.36			
S	R^2	*Adj-*R^2			
2.71	0.9611	0.9222			
AMP					
Model	6	7.78	1.30	27.64	<0.001
Linear	5	7.74	1.55	32.97	<0.001
Adsorbent amount (mg)	1	1.96	1.96	41.68	0.001
Adsorption time (min)	1	0.37	0.37	7.77	0.032
Initial concentration (ng mL^{-1})	1	2.65	2.65	56.54	<0.001
Sample volume (mL)	1	1.52	1.52	32.46	0.001
NaCl content (mol L^{-1})	1	1.24	1.24	26.41	0.002
Curvature	1	0.05	0.05	0.99	0.357
Error	6	0.28	0.05		
Total	12	8.0654			
S	R^2	*Adj-*R^2			
2.17	0.9651	0.9302			
MEAM					
Model	6	6.14	1.02	27.14	<0.001
Linear	5	6.07	1.22	32.20	<0.001
Adsorbent amount (mg)	1	1.33	1.33	35.38	0.001
Adsorption time (min)	1	0.30	0.30	7.83	0.031
Initial concentration (ng mL^{-1})	1	2.33	2.33	61.85	<0.001
Sample volume (mL)	1	0.75	0.75	19.91	0.004
NaCl content (mol L^{-1})	1	1.36	1.36	36.07	0.001
Curvature	1	0.07	0.07	1.81	0.227
Error	6	0.23	0.04		
Total	12	6.37			

S	R^2	*Adj*-R^2			
1.94	0.9645	0.9289			
MOR					
Model	6	13.99	2.33	7.37	0.014
Linear	5	13.99	2.80	8.84	0.01
Adsorbent amount (mg)	1	3.44	3.44	10.85	0.017
Adsorption time (min)	1	0.87	0.87	2.73	0.149
Initial concentration (ng mL^{-1})	1	0.40	0.40	1.27	0.303
Sample volume (mL)	1	9.13	9.13	28.83	0.002
NaCl content (mol L^{-1})	1	0.16	0.16	0.49	0.509
Curvature	1	0.009	0.009	0.03	0.874
Error	6	1.90	0.32		
Total	12	15.90			
S	R^2	*Adj*-R^2			
5.63	0.8805	0.7610			
PAP					
Model	6	1.17	0.20	1.51	0.315
Linear	5	1.13	0.23	1.74	0.258
Adsorbent amount (mg)	1	0.42	0.42	3.27	0.121
Adsorption time (min)	1	0.01	0.01	0.09	0.769
Initial concentration (ng mL^{-1})	1	0.05	0.05	0.36	0.57
Sample volume (mL)	1	0.58	0.58	4.52	0.078
NaCl content (mol L^{-1})	1	0.06	0.06	0.47	0.519
Curvature	1	0.04	0.04	0.34	0.58
Error	6	0.77	0.13		
Total	12	1.94			
S	R^2	*Adj*-R^2			
3.59	0.6016	0.2031			
THE					
Model	6	10.34	1.72	39.80	<0.001
Linear	5	10.26	2.05	47.40	<0.001
Adsorbent amount (mg)	1	4.03	4.03	93.14	<0.001
Adsorption time (min)	1	0.23	0.23	5.33	0.06
Initial concentration (ng mL^{-1})	1	0.0006	0.0006	0.01	0.909
Sample volume (mL)	1	5.99	5.99	138.51	<0.001
NaCl content (mol L^{-1})	1	0.00	0.00	0.00	0.989
Curvature	1	0.08	0.08	1.82	0.226
Error	6	0.26	0.04		
Total	12	10.60			
S	R^2	*Adj*-R^2			
2.08	0.9755	0.9510			

Table S4. Analysis of variance (ANOVA) for quadratic model (six PAS).

Factors	Sum of Squares	d_f	Mean Square	*F*-value	*p*-value
EPH					
Model	3379.76	9	375.53	18.02	0.0005
X_1	1149.38	1	1149.38	55.15	0.0001
X_2	506.27	1	506.27	24.29	0.0017
X_3	1327.58	1	1327.58	63.70	< 0.0001
X_1X_2	290.4	1	290.4	13.93	0.0073
X_1X_3	22.98	1	22.98	1.10	0.3286
X_2X_3	54.64	1	54.64	2.62	0.1495
X_1^2	22.79	1	22.79	1.09	0.3305
X_2^2	2.7	1	2.70	0.13	0.7296
X_3^2	4.47	1	4.47	0.21	0.6573
Residual	145.89	7	20.84		
Lack of Fit	129.12	3	43.04	10.27	0.0238
Std. Dev.	C.V. %	R^2	$Adj\text{-}R^2$		
4.57	7.65	0.9586	0.9054		
MEEP					
Model	4697.14	9	521.9	14.79	0.0009
X_1	2277.47	1	2277.47	64.52	< 0.0001
X_2	623.59	1	623.59	17.67	0.004
X_3	1460.68	1	1460.68	41.38	0.0004
X_1X_2	47.67	1	47.67	1.35	0.2833
X_1X_3	91.65	1	91.65	2.60	0.1511
X_2X_3	65.11	1	65.11	1.84	0.2166
X_1^2	121.53	1	121.53	3.44	0.1059
X_2^2	7.09	1	7.09	0.20	0.6675
X_3^2	7.36	1	7.36	0.21	0.6618
Residual	247.08	7	35.30		
Lack of Fit	192.68	3	64.23	4.72	0.0839
Std. Dev.	C.V. %	R^2	$Adj\text{-}R^2$		
5.94	11.04	0.9500	0.8858		
AMP					
Model	1399.87	9	155.54	22.83	0.0002
X_1	569.4	1	569.4	83.58	< 0.0001
X_2	387.87	1	387.87	56.93	0.0001
X_3	253.55	1	253.55	37.22	0.0005
X_1X_2	7.44	1	7.44	1.09	0.3309
X_1X_3	68.93	1	68.93	10.12	0.0155
X_2X_3	12	1	12.00	1.76	0.2261
X_1^2	99.71	1	99.71	14.64	0.0065
X_2^2	0.19	1	0.19	0.03	0.8706

X_3^2	0.15	1	0.15	0.02	0.8855
Residual	47.69	7	6.81		
Lack of Fit	40.33	3	13.44	7.31	0.0423
Std. Dev.	C.V. %	R^2	$Adj\text{-}R^2$		
2.61	2.95	0.9671	0.9247		
MEAM					
Model	11063.59	9	1229.29	328.31	< 0.0001
X_1	194.89	1	194.89	52.05	0.0002
X_2	5669.32	1	5669.32	1514.13	< 0.0001
X_3	120.11	1	120.11	32.08	0.0008
X_1X_2	34.47	1	34.47	9.21	0.019
X_1X_3	32.89	1	32.89	8.78	0.021
X_2X_3	17.03	1	17.03	4.55	0.0704
X_1^2	25.9	1	25.9	6.92	0.0339
X_2^2	4868.3	1	4868.3	1300.2	< 0.0001
X_3^2	8.19	1	8.19	2.19	0.1826
Residual	26.21	7	3.74		
Lack of Fit	21.46	3	7.15	6.02	0.0578
Std. Dev.	C.V. %	R^2	$Adj\text{-}R^2$		
1.94	2.6	0.9976	0.9946		
PAP					
Model	4683.56	9	520.4	20.63	0.0003
X_1	1226.83	1	1226.83	48.64	0.0002
X_2	30.08	1	30.08	1.19	0.311
X_3	2979.38	1	2979.38	118.13	< 0.0001
X_1X_2	63.51	1	63.51	2.52	0.1566
X_1X_3	74.45	1	74.45	2.95	0.1295
X_2X_3	11.48	1	11.48	0.46	0.5215
X_1^2	10.3	1	10.3	0.41	0.5432
X_2^2	0.24	1	0.24	9.34E-03	0.9257
X_3^2	290.89	1	290.89	11.53	0.0115
Residual	176.55	7	25.22		
Lack of Fit	110.98	3	36.99	2.26	0.2239
Std. Dev.	C.V. %	R^2	$Adj\text{-}R^2$		
5.02	12.46	0.9637	0.917		
THE					
Model	2942.04	9	326.89	18.24	0.0005
X_1	813.68	1	813.68	45.40	0.0003
X_2	0.53	1	0.53	0.029	0.8687
X_3	1875.04	1	1875.04	104.62	< 0.0001
X_1X_2	8.97	1	8.97	0.50	0.5021
X_1X_3	3.99	1	3.99	0.22	0.6515
X_2X_3	24.81	1	24.81	1.38	0.2779

X_1^2	8.52	1	8.52	0.48	0.5127
X_2^2	104.79	1	104.79	5.85	0.0462
X_3^2	112.65	1	112.65	6.29	0.0406
Residual	125.45	7	17.92		
Lack of Fit	94.75	3	31.58	4.11	0.1027
Std. Dev.	C.V. %	R^2	*Adj-R*^{2}		
4.23	7.11	0.9591	0.9065		

X_1: Adsorbent amount (mg); X_2: Initial concentration (ng mL^{-1}); X_3: Sample volume (mL).

Table S5. Summary of kinetic parameters of PAS adsorption.

Models and Parameters	EPH	MEEP	AMP	MEAM	MOR	PAP	THE
Pseudo first order							
Q_e	13.503	17.468	21.073	24.135	11.551	16.030	21.455
K_1	0.078	0.036	1.308	1.381	0.117	3.721	1.168
R^2	0.829	0.927	0.770	0.815	0.771	0.984	0.79
Pseudo second order							
Q_e	14.374	19.380	21.94	25.016	12.128	16.219	22.292
K_2	0.009	0.003	0.081	0.081	0.018	0.644	0.075
R^2	0.907	0.926	0.855	0.899	0.873	0.994	0.875
Elovich							
a	13.160	6.792	3017.617	1382.727	20.889	626.606	3009.523
b	0.508	0.372	0.528	0.516	0.655	2.703	0.521
R^2	0.983	0.945	0.993	0.997	0.988	0.997	0.996

Table S6. Summary of isotherm parameters of PAS adsorption.

Models and Parameters	EPH	MEEP	AMP	MEAM	MOR	PAP	THE
Langmuir							
Q_m	68.047	48.669	129.244	101.096	103.272	84.336	64.217
K_L	0.002	0.003	0.001	0.002	0.002	0.002	0.002
R^2	0.999	0.995	0.993	0.995	0.998	0.994	0.949
Freundlich							
K_F	0.366	0.549	0.315	0.457	0.544	0.752	0.287
$1/n$	0.720	0.634	0.797	0.739	0.722	0.661	0.748
R^2	0.991	0.992	0.994	0.989	0.993	0.995	0.955
Temkin							
B	7.634	6.493	10.412	10.616	11.565	10.665	7.235
K_T	0.065	0.079	0.061	0.064	0.064	0.074	0.059
R^2	0.862	0.887	0.812	0.847	0.871	0.888	0.808

Table S7. The bond assignment and binding energy after and before adsorption of PAS.

Elements		After adsorption	Before adsorption
	Bond assignment	Binding energy (eV)	Binding energy (eV)
C 1s	C−C/C=C	284.7	284.8
	C−N	285.7	285.8
	C−O	287.1	286.5
	C=O	289.8	289.9
N 1s	C=N−	399	398.9
	C−NH−	399.3	399.5
O 1s	C=O	531.7	531.6
	C−O	532.5	532.6
	Fe−O	529.9	529.8
Zn	Zn $2p_{1/2}$	1045.1	1045.0
	Zn $2p_{3/2}$	1022.0	1021.9

Table S8. Comparison of different methods for analysis of PAS in water sample.

Method	Detection	Optimization	Recovery (%)	Linearity (ng mL^{-1})	LODs (ng mL^{-1})	LOQs (ng mL^{-1})	RSDs (%)	Ref.
MSPE	UHPLC-MS/MS	DOE	74.92-94.47	1-100	0.09-0.35	0.29-1.18	0.06-2.21	This work
Online-SPE	LC-MS/MS	[a]	80-120	0.1-2000	7-69 ng L^{-1}	23-228 ng L^{-1}	<13	[22]
SPE	UHPLC-MS/MS	OFAT	65-137	0.1-1500	-	0.2-30	0.6-13	[23]
SPE	LC-MS/MS	OFAT	70-98	30-5000 ng L^{-1}	-	-	<23	[24]
SPE	UHPLC-MS/MS	[a]	70-120	2-70	0.05-30 ng L^{-1}	-	<20	[25]
SPE	μLC-MS/MS	[a]	75-119	4–2000 ng L^{-1}	-	3-70 ng L^{-1}	1-16	[26]
SPE	LC-MS	[a]	30-107	0.14-2.81 ng L^{-1}	0.01-1.9 ng L^{-1}	0.02-3.64 ng L^{-1}	<15	[27]
SPE	LC-MS/MS	[a]	101-121	0.2-80	0.3-18 ng L^{-1}[b]	0.9-60 ng L^{-1}[b]	<13	[28]
SPE	LC-MS	[a]	70-120	1.8-720 ng L^{-1}[b]	-	2-35 ng L^{-1}[b]	<30	[29]
LLE	UHPSFC-MS/MS	OFAT	62-122	0.5-100	0.02-4.28	1-59 ng L^{-1}	2.1-17.8	[30]
FaDEx	GC-FID	OFAT	85.4-110.2	20-2000	4	20	≤8	[31]

MSPE: Magnetic solid phase extraction; UHPLC-MS/MS: Ultra-high performance liquid chromatography tandem mass spectrometry; SPE: Solid phase extraction; LC-MS/MS: Liquid chromatography tandem mass spectrometry; DOE: Design of experiments; OFAT: One factorial at a time; μLC-MS/MS: Micro liquid chromatography tandem mass spectrometry; LC-MS: liquid chromatography mass spectrometry; LLE: Liquid-liquid extraction; UHPSFC-MS/MS: Ultra-high performance supercritical fluid chromatography-tandem mass spectrometry. FaDEx: Fast drug extraction. GC-FID: gas chromatography-flame ionization detection.

[a] The optimization process of preprocessing are not mentioned in paper.

[b] Information in effluent wastewater samples.

Reference

1 S.R. Cao, T.T. Tang, C.X. Xi and Z.Q. Chen, Fabricating magnetic GO/ZIF-8 nanocomposite for amphetamine adsorption from water: Capability and mechanism, *Chem. Eng. J.*, 2021, 422, 130096.

2 M. Thommes, Physisorption of gases, with special reference to the evaluation of surface area and pore size distribution (IUPAC Technical Report), *Pure Appl. Chem.*, 2016, 87, 25-25.

3 A.I.A. Sherlala, A.A.A. Ramana, M.M. Bello and A. Buthiyappan, Adsorption of arsenic using chitosan magnetic graphene oxide nanocomposite, *J Environ Manage.*, 2019, 246, 547-556.

4 Z. Bohstrom and K.P. Lillerud, Preparation of chabazite with mesopores templated from a cationic polymer, *Microporous Mesoporous Mater.*, 2018, 271, 295-300.

5 L. Chen, J. Peng, F.Q. Wang, D.H. Liu, W.R. Ma, J.M. Zhang, W.Q. Hu, N. Li, P. Dramou and H. He, ZnO nanorods/Fe_3O_4-graphene oxide/metal-organic framework nanocomposite: recyclable and robust photocatalyst for degradation of pharmaceutical pollutants, Environ Sci Pollut Res Int., 2021, 28, 21799-21811.

6 J. Peng, H. Tian, Q.Z. Du, X.H. Hui and H. He, A regenerable sorbent composed of a zeolite imidazolate framework (ZIF-8), Fe_3O_4 and graphene oxide for enrichment of atorvastatin and simvastatin prior to their determination by HPLC, Mikrochim Acta, 2018, 185, 141-150.

7 S. Aytas, S. Yusan, S. Sert and C. Gok, Preparation and characterization of magnetic graphene oxide nanocomposite (GO-Fe_3O_4) for removal of strontium and cesium from aqueous solutions, Compos. Mater. Res., 2021, 6, 26-42.

8 J.B. Wu, M.L. Lin, X. Cong, H.N. Liu and P.H. Tan, Raman spectroscopy of graphene-based materials and its applications in related devices, Chem Soc Rev., 2018, 47, 1822-1873.

9 M. Muniyalakshmi, K. Sethuraman and D. Silambarasan, Synthesis and characterization of graphene oxide nanosheets, *Mater. Today: Proceedings*, 2020, 21, 408-410.

10 L. Zeng, D. Cheng, Z. Mao, Y. Zhou and T. Jing, ZIF-8/nitrogen-doped reduced graphene oxide as thin film microextraction adsorbents for simultaneous determination of novel halogenated flame retardants in crayfish-aquaculture water systems, *Chemosphere*, 2022, 287, 132408.

11 J. Peng, H. Tian, Q. Du, X. Hui and H. He, A regenerable sorbent composed of a zeolite

imidazolate framework (ZIF-8), Fe_3O_4 and graphene oxide for enrichment of atorvastatin and simvastatin prior to their determination by HPLC, *Mikrochim Acta*, 2018, 185, 141.

12 J. Wang, Y. Li, Z. Lv, Y. Xie, J. Shu, A. Alsaedi, T. Hayat and C. Chen, Exploration of the adsorption performance and mechanism of zeolitic imidazolate framework-8@graphene oxide for Pb(II) and 1-naphthylamine from aqueous solution, *J. Colloid. Interface Sci.*, 2019, 542, 410-420.

13 Y. Chen and S. Tang, Solvothermal synthesis of porous hydrangea-like zeolitic imidazole framework-8 (ZIF-8) crystals, *J. Solid. State. Chem.*, 2019, 276, 68-74.

14 Y. Wong, Y. Szeto, W. Cheung and G. McKay, Pseudo-first-order kinetic studies of the sorption of acid dyes onto chitosan, J. Appl. Polym. Sci., 2004, 92, 1633-1645.

15 Y.S. Ho, Review of second-order models for adsorption systems, J. Hazard Mater.,2006, 136, 681-689.

16 O. Aksakal and H. Ucun, Equilibrium, kinetic and thermodynamic studies of the biosorption of textile dye (Reactive Red 195) onto Pinus sylvestris L, J. Hazard Mater.,2010, 181, 666-672.

17 I. Langmuir, The adsorption of gases on plane surfaces of glass, mica and platinum, J. Am. Chem. Soc.,1918, 40, 1361-1403.

18 M.D. LeVan and T. Vermeulen, Binary Langmuir and Freundlich isotherms for ideal adsorbed solutions, J. Phys. Chem.,1981, 85, 3247-3250.

19 M. Wawrzkiewicz and Z. Hubicki, Equilibrium and kinetic studies on the adsorption of acidic dye by the gel anion exchanger, J. Hazard Mater.,2009, 172, 868-874.

20 H.M. Jang, S. Yoo, Y.K. Choi, S. Park and E. Kan, Adsorption isotherm, kinetic modeling and mechanism of tetracycline on Pinus taeda-derived activated biochar, Bioresour Technol., 2018, 259, 24-31.

21 Y. Ma, L. Wu, P. Li, L. Yang, L. He, S. Chen, Y. Yang, F. Gao, X. Qi and Z. Zhang, A novel, efficient and sustainable magnetic sludge biochar modified by graphene oxide for environmental concentration imidacloprid removal, J Hazard Mater., 2021, 407, 124777.

22 E. López-García, N. Mastroianni, C. Postigo, D. Barceló, and López de Alda, A fully automated approach for the analysis of 37 psychoactive substances in raw wastewater based on on-line solid phase extraction-liquid chromatography-tandem mass spectrometry, *J.*

Chromatogr A, 2018, 1576, 80-89.

23 I. González-Mariño, V. Castro, R. Montes, R. Rodil, A. Lores, R. Cela and J.B. Quintana, Multi-residue determination of psychoactive pharmaceuticals, illicit drugs and related metabolites in wastewater by ultra-high performance liquid chromatography-tandem mass spectrometry, *J. Chromatogr A*, 2018, 1569, 91-100.

24 N. Gilart, P.A. Cormack, R.M. Marcé, N. Fontanals and F. Borrull, Selective determination of pharmaceuticals and illicit drugs in wastewaters using a novel strong cation-exchange solid-phase extraction combined with liquid chromatography-tandem mass spectrometry, *J. Chromatogr A*, 2014, 1325, 137-46.

25 L. Bijlsma, J.V. Sancho, E. Pitarch, M. Ibáñez and F. Hernández, Simultaneous ultra-high-pressure liquid chromatography-tandem mass spectrometry determination of amphetamine and amphetamine-like stimulants, cocaine and its metabolites, and a cannabis metabolite in surface water and urban wastewater, *J. Chromatogr A*. 1216 (2009) 3078-3089.

26 A. Celma, J.V. Sancho, N. Salgueiro-González, S. Castiglioni, E. Zuccato, F. Hernández and L. Bijlsma, Simultaneous determination of new psychoactive substances and illicit drugs in sewage: Potential of micro-liquid chromatography tandem mass spectrometry in wastewater-based epidemiology, *J. Chromatogr A*, 2019, 1602, 300-309.

27 Y. Peng, L. Gautam and S.W. Hall, The detection of drugs of abuse and pharmaceuticals in drinking water using solid-phase extraction and liquid chromatography-mass spectrometry. *Chemosphere*, 2019, 223, 438-447.

28 V.L. Borova, P. Gago-Ferrero, C. Pistos and N.S. Thomaidis, Multi-residue determination of 10 selected new psychoactive substances in wastewater samples by liquid chromatography-tandem mass spectrometry, *Talanta*, 2015, 144, 592-603.

29 R. Diaz, M. Ibá˜nez, J.V. Sancho and F. Hernández, Qualitative validation of a liquid chromatography–quadrupole-time of flight mass spectrometry screening method for organic pollutants in waters, *J. Chromatogr A*, 2013, 1276, 47-57.

30 I. González-Mariño, K.V. Thomas and M.J. Reid, Determination of cannabinoid and synthetic cannabinoid metabolites in wastewater by liquid-liquid extraction and ultra-high performance supercritical fluid chromatography-tandem mass spectrometry, *Drug Test Anal.*, 2018, 10, 222-228.

31 S. Gurrani, K. Prakasham, J.L. Zii Ying, J. Shiea, Y.J. Ku, Y.C. Lin, P.C. Huang, G. Andaluri, K.C. Lee and V.K. Ponnusamy, A low-cost eco-friendly fast drug extraction (FaDEx) technique for environmental and bio-monitoring of psychoactive drug in urban water and sports-persons' urine samples, *Environ Res.*, 2023, 217, 114787.